

Temperature and Field Dependence of Ferromagnetic Magnon in Monolayer Honeycomb Spin Lattice

Niem T. Nguyen¹, Giang H. Bach¹, Thao H. Pham², Huy D. Nguyen¹,
Oanh T. K. Nguyen³, Cong T. Bach¹

¹*Faculty of Physics, University of Science, Vietnam National University,
334 Nguyen Trai street, Thanh Xuan, Hanoi, Vietnam*

²*Hue University, 34 Le Loi, Hue, Vietnam*

³*Electric Power University, 235 Hoang Quoc Viet street, Bac Tu Liem, Hanoi, Vietnam*

Abstract

Temperature and field dependence of collective spin excitations or magnon in monolayer honeycomb spin lattices is investigated using an anisotropic exchange XZ-Heisenberg model in an external field. Magnetic phase transition in the presence of the transverse field is the spin reorientation (SR) transition with magnon intensity existing above the SR temperature. The transverse field either decreases or sustains the spin-wave intensity in the temperature region below or above the SR temperature, respectively. The gap of the zero-momentum low-energy magnon branch closes at the SR transverse field, which is the critical quantum phase transition field at zero temperature. The application of the model to a two-dimensional CrI₃ explains the existence of the zero-momentum magnon mode above the Curie temperature and shows the suitable values of the exchange parameters compared with the DFT calculations. The estimated magnon velocity near the Dirac point in this material is about 1.74 km/s.

Keywords: ferromagnetic magnon, quantum phase transition, Dirac

1. Introduction

Dirac materials having elementary excitation spectra similar to the Dirac electronic quasiparticle in graphene are intensively investigated for the last decade [1]. Among the Dirac fermion, Dirac bosons such as magnon in honeycomb structural magnets have drawn great attention to both fundamental and practical research. It is shown that due to the spatial symmetry of the honeycomb spin-lattice, the magnon energy spectra have a Dirac-like dispersion either around the K and K' points of the Brillouin zone (BZ) for the ferromagnetic (FM) magnon or around the center of the BZ for the antiferromagnetic (AF) magnon [2, 3]. It is also proposed that competing interactions in the FM structure induce Dirac and Weyl points while Dirac nodes relate to the magnetic structure but not to the overall crystal symmetry [4].

Based on graphene-like two-dimensional (2D) materials, Van der Waals crystal chromium triiodide CrI_3 , one of the typical 2D magnets, exhibits ferromagnetic order when the size of the crystal is down to a single layer [5, 6]. Acoustical and optical magnon branches are recognized in the mono-layer CrI_3 using magneto-Raman spectroscopy [7]. Temperature dependence of the two branches of the zero-momentum magnon ($k=0$) has been experimentally investigated in the 2D honeycomb ferromagnet CrI_3 [8] and analyzed by the anisotropic Heisenberg model. It is indicated that the magnon energy reduces with increasing temperature below the phase transition temperature (T_C), whereas it remains finite, and nearly temperature-independent above this. In the framework of the XZ-Heisenberg model with the transverse field

(TF), the spin wave in the monolayer square spin-lattice can exist above T_C and displays a weak temperature dependence [9]. The phase transition temperature in the presence of the TF can be interpreted as the spin reorientation (SR) temperature following Ref. [10]. This transition due to the TF at zero temperature belongs to quantum phase transition (QPT) where the TR plays a role of tuning parameters which probably are pressure, doping fraction, in-plane stress, etc. [11].

The longitudinal magnetic-field-induced quantum phase transition was experimentally explored in the CrI_3 bulk with honeycomb spin structure, where antiferromagnetic surface layers transformed to a ferromagnetic (FM) state at the critical field of about 2 T [12]. The magnetic phase transitions in the single CrI_3 layer induced by stress due to in-plane lattice deformation are theoretically examined in Ref. [13]. The temperature-independent magnon intensity above the phase transition temperature [8] was particularly described by the spin-wave theory in the XZ-Heisenberg model with the TF which mimics the in-plane stress [9]. According to our knowledge, the finite temperature and transverse field behaviors of the honeycomb spin-lattice FM magnon have received relatively modest attention.

For this reason, we aim to deeply understand the temperature and the TF behavior of the monolayer honeycomb spin-lattice magnons, including the QPT case. Our results bring specific features of magnon energy in the CrI_3 and other 2D systems observed in experiments. The paper is organized as follows: the next part describes the model and the calculation method. In Section III, we analyze the FM magnon spectra in the monolayer honeycomb spin-lattice and compare our model parameters with experimental

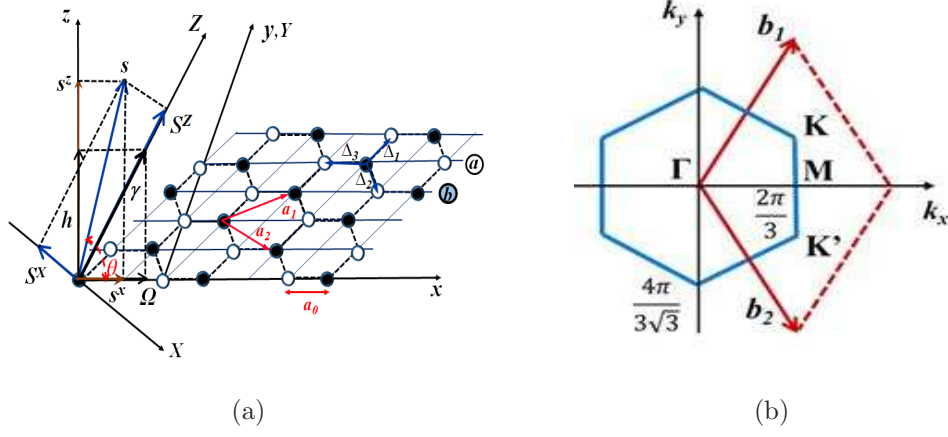


Figure 1: Orientation of a spin in the honeycomb spin-lattice relates to the crystallographic (xyz) and rotated (XYZ) coordinate systems (a) and the first Brillouin zone (b).

calculations. We will summarize our results in the conclusion part.

2. XZ-Heisenberg model and Green function

2.1. Hamiltonian of the XZ- Heisenberg model for monolayer films

We consider a monolayer honeycomb spin-lattice consisting of $2N$ spins residing in two triangular a and b spin sub-lattices shown in Fig. 1(a). Position vectors of these spins in the sub-lattices are denoted by two-dimensional lattice vectors \mathbf{j} and \mathbf{g} . Three nearest-neighbors (NN) of an a -spin at site \mathbf{j} are b -spins defined by three vectors Δ which are $\Delta_1 = \frac{a_0}{2}(3, \sqrt{3})$, $\Delta_2 = \frac{a_0}{2}(3, -\sqrt{3})$, $\Delta_3 = \frac{a_0}{2}(-1, 0)$ with the length of the hexagonal edge a_0 . Similarly, three NN of a b -spin at site \mathbf{g} are a -spins positioned by vectors $-\Delta$. The six next-nearest-neighbors (NNN) of the $a(b)$ -sub-lattice are the same spin types defined by vectors $\rho_1 = \frac{a_0}{2}(3, \sqrt{3}) = -\rho_4$, $\rho_2 = \frac{a_0}{2}(3, -\sqrt{3}) = -\rho_5$, $\rho_3 = \frac{a_0}{2}(0, -\sqrt{3}) = -\rho_6$.

The Hamiltonian of the XZ–Heisenberg model for the honeycomb mono-layer spin-lattice in the external fields is written by

$$\begin{aligned}
H = & - \sum_{\mathbf{j}} (h_0 s_{\mathbf{aj}}^z + \Omega_0 s_{\mathbf{aj}}^x) - \sum_{\mathbf{g}} (h_0 s_{\mathbf{bg}}^z + \Omega_0 s_{\mathbf{bg}}^x) - \frac{1}{2} \sum_{\mathbf{j}, \Delta} (J s_{\mathbf{aj}}^z s_{\mathbf{b}, \mathbf{j}+\Delta}^z + L s_{\mathbf{aj}}^x s_{\mathbf{b}, \mathbf{j}+\Delta}^x) \\
& - \frac{1}{2} \sum_{\mathbf{g}, \Delta} (J s_{\mathbf{bg}}^z s_{\mathbf{a}, \mathbf{g}-\Delta}^z + L s_{\mathbf{bg}}^x s_{\mathbf{a}, \mathbf{g}-\Delta}^x) - \frac{1}{2} \sum_{\mathbf{j}, \rho} J' (s_{\mathbf{aj}}^z s_{\mathbf{b}, \mathbf{j}+\rho}^z + s_{\mathbf{aj}}^x s_{\mathbf{b}, \mathbf{j}+\rho}^x) \\
& - \frac{1}{2} \sum_{\mathbf{g}, \rho} J' (s_{\mathbf{bg}}^z s_{\mathbf{a}, \mathbf{g}-\rho}^z + s_{\mathbf{bg}}^x s_{\mathbf{a}, \mathbf{g}-\rho}^x) \quad (1)
\end{aligned}$$

Here h_0, Ω_0 are the external longitudinal and transverse field intensity given in the energy unit. The components of sub-lattice spin operators in the crystallographic xyz frame, where the z -axis is perpendicular to the honeycomb spin-lattice plane, are denoted by $s_{\mathbf{aj}}^z, s_{\mathbf{aj}}^x, s_{\mathbf{bg}}^z, s_{\mathbf{bg}}^x$. J and L are NN exchange parameters between spin-pair components along the out-of-plane z and in-plane x directions, respectively. Since long-range order generally does not exist in a 2D isotropic exchange Heisenberg model [14], the exchange parameters are chosen as $J \neq L$. J' is the NNN exchange between spins of the same types.

Using the mean-field approximation (MFA), we rewrite the Hamiltonian (1) in terms of spin fluctuation operators $\delta s_{a(b)\mathbf{j}}^z = s_{a(b)\mathbf{j}}^z - m_{az(bz)}$,

$$H = H_0 + H_1, \quad (2)$$

where

$$\begin{aligned}
H_0 = & 3N [J m_{az} m_{bz} + L m_{ax} m_{bx} + J' (m_a^2 + m_b^2)] \\
& - \sum_{\mathbf{j}} (h_a s_{\mathbf{aj}}^z + \Omega_a s_{\mathbf{aj}}^x) - \sum_{\mathbf{g}} (h_b s_{\mathbf{bg}}^z + \Omega_b s_{\mathbf{bg}}^x), \quad (3)
\end{aligned}$$

$$H_1 = -\frac{1}{2} \sum_{\mathbf{j}, \Delta} (J \delta s_{\mathbf{aj}}^z \delta s_{\mathbf{b}, \mathbf{j}+\Delta}^z + L \delta s_{\mathbf{aj}}^x \delta s_{\mathbf{b}, \mathbf{j}+\Delta}^x)$$

$$\begin{aligned}
& - \frac{1}{2} \sum_{\mathbf{g}\Delta} (J\delta s_{a\mathbf{g}}^z \delta s_{b,\mathbf{g}-\Delta}^z + L\delta s_{a\mathbf{g}}^x \delta s_{b,\mathbf{g}-\Delta}^x) \\
& - \frac{1}{2} \sum_{\mathbf{j}\rho} J'(\delta s_{a\mathbf{j}}^z \delta s_{b,\mathbf{j}+\rho}^z + \delta s_{a\mathbf{j}}^x \delta s_{b,\mathbf{j}+\rho}^x) \\
& - \frac{1}{2} \sum_{\mathbf{g}\rho} J'(\delta s_{a\mathbf{g}}^z \delta s_{b,\mathbf{g}-\rho}^z + L\delta s_{a\mathbf{g}}^x \delta s_{b,\mathbf{g}-\rho}^x),
\end{aligned} \tag{4}$$

and

$$\begin{aligned}
h_{a(b)} &= h_0 + 3Jm_{bz(az)} + 6J'm_{az(bz)}, \\
\Omega_{a(b)} &= \Omega_0 + 3Lm_{bx(ax)} + 6J'm_{ax(bx)}.
\end{aligned} \tag{5}$$

Here $m_{\nu x} = \langle s_{\nu}^x \rangle$, $m_{\nu z} = \langle s_{\nu}^z \rangle$ with $\nu = a, b$ are thermodynamic average of the spin-moment components per site and $m_{\nu} = \sqrt{m_{\nu x}^2 + m_{\nu z}^2}$, and $\langle \dots \rangle = \text{Tr}(e^{-\beta H} \dots) / \text{Tr}(e^{-\beta H})$. The formula (5) produces the longitudinal and transverse components, h_{ν} and Ω_{ν} , of the net field acting on the ν -sub-lattice. The Hamiltonian H_0 is diagonalized using the transformation,

$$\begin{aligned}
s_{\nu\mathbf{j}}^x &= \frac{h_{\nu}}{\gamma_{\nu}} S_{\nu\mathbf{j}}^X + \frac{\Omega_{\nu}}{\gamma_{\nu}} S_{\nu\mathbf{j}}^Z, \\
s_{\nu\mathbf{j}}^z &= -\frac{\Omega_{\nu}}{\gamma_{\nu}} S_{\nu\mathbf{j}}^X + \frac{h_{\nu}}{\gamma_{\nu}} S_{\nu\mathbf{j}}^Z.
\end{aligned} \tag{6}$$

During the transformation, spin fluctuation operators $\delta s_{\nu\mathbf{j}}^{\alpha}$ ($\alpha = x, z$) are transformed to new operators $\delta S_{\nu\mathbf{j}}^{\alpha} = S_{\nu\mathbf{j}}^{\alpha} - \langle S_{\nu}^{\alpha} \rangle$, ($\alpha = X, Z$). Performing Fourier transformation $\delta S_{\nu\mathbf{j}}^{\alpha} = N^{-1/2} \sum_{\mathbf{k}} \delta S_{\nu}^{\alpha}(\mathbf{k}) e^{i\mathbf{k}\mathbf{j}}$ with two-dimensional wave vector \mathbf{k} defined in the first Brillouin zone (shown in Fig. 1(b)), we rewrite the Hamiltonian (3) and (4) as

$$H_0 = 3N \{ Jm_{az}m_{bz} + Lm_{ax}m_{bx} + J'(m_a^2 + m_b^2) \} - \sum_{\nu\mathbf{j}} \gamma_{\nu} S_{\nu\mathbf{j}}^z, \tag{7}$$

and

$$H_1 = -\frac{1}{2} \sum_{\mathbf{k}} \sum_{\lambda\lambda'} I_{\lambda\lambda'}(\mathbf{k}) \delta S^{\lambda}(\mathbf{k}) \delta S^{\lambda'}(-\mathbf{k}), \tag{8}$$

where λ and λ' run from 1 to 4 meaning $1 \equiv aX$, $2 \equiv aZ$, $3 \equiv bX$, $4 \equiv bZ$.

The anisotropic exchange interaction is a Hermitian matrix defined by

$$\hat{I}(\mathbf{k}) = \begin{pmatrix} \xi_{2\mathbf{k}} & 0 & C\xi_{1\mathbf{k}}^* & D\xi_{1\mathbf{k}}^* \\ 0 & \xi_{2\mathbf{k}} & \tilde{D}\xi_{1\mathbf{k}}^* & \tilde{C}\xi_{1\mathbf{k}}^* \\ C\xi_{1\mathbf{k}} & \tilde{D}\xi_{1\mathbf{k}} & \xi_{2\mathbf{k}} & 0 \\ D\xi_{1\mathbf{k}} & \tilde{C}\xi_{1\mathbf{k}} & 0 & \xi_{2\mathbf{k}} \end{pmatrix}, \quad (9)$$

where

$$C = \frac{(J\Omega_a\Omega_b + Lh_a h_b)}{\gamma_a \gamma_b}, \quad \tilde{C} = \frac{(L\Omega_a\Omega_b + Jh_a h_b)}{\gamma_a \gamma_b}, \quad (10)$$

$$D = \frac{(-J\Omega_a h_b + L\Omega_b h_a)}{\gamma_a \gamma_b}, \quad \tilde{D} = \frac{(L\Omega_a h_b - J\Omega_b h_a)}{\gamma_a \gamma_b}, \quad (11)$$

and

$$\begin{aligned} \xi_{1\mathbf{k}} &= \sum_{\Delta} e^{i\mathbf{k}\Delta} = e^{-ik_x a_0} (1 + 2e^{i3k_x a_0/2} \cos(\sqrt{3}k_y a_0/2)), \\ \xi_{2\mathbf{k}} &= \sum_{\rho} e^{i\mathbf{k}\rho} = 4\cos(3k_x a_0/2)\cos(\sqrt{3}k_y a_0/2) + 2\cos(\sqrt{3}k_y a_0). \end{aligned} \quad (12)$$

2.2. Green's functions

The temperature and field dependence of the magnon spectra is obtained from the poles of the imaginary time Green's function (GF) as carried out in Ref. [9]. The Green's function basing on the spin fluctuation operators $\delta s_{\nu j}^{\alpha}$ ($\alpha = x, z$; $\nu = a, b$) given in the crystallographic spin-lattice coordinates and in the Heisenberg picture is written as

$$G_{\nu\nu'}^{\alpha\alpha'}(\mathbf{j} - \mathbf{j}', \tau_1 - \tau_2) = \langle \hat{T} \delta \tilde{s}_{\mathbf{j}\nu}^{\alpha}(\tau_1) \delta \tilde{s}_{\mathbf{j}'\nu'}^{\alpha'}(\tau_2) \rangle, \quad (13)$$

where

$$\delta \tilde{s}_{\mathbf{j}\nu}^{\alpha}(\tau) = e^{\tau H} \delta s_{\mathbf{j}\nu}^{\alpha} e^{-\tau H}. \quad (14)$$

Taking Fourier transformation of the GF, we have

$$G_{\nu\nu'}^{\alpha\alpha'}(\mathbf{j} - \mathbf{j}', \tau) = \frac{1}{N} \sum_{\mathbf{k}\omega} G_{\nu\nu'}^{\alpha\alpha'}(\mathbf{k}, \omega) e^{-i\mathbf{k}(\mathbf{j}-\mathbf{j}')-i\omega\tau}, \quad (15)$$

where $\omega = 2\pi n/\beta$; $n = 0, \pm 1, \pm 2, \dots$. Denoting (\mathbf{k}, ω) as the three-component wave vector \mathbf{q} and putting $\mathbf{R} = \mathbf{j} - \mathbf{j}'$, the Fourier image of the GF writes

$$\begin{aligned} G_{\nu\nu'}^{\alpha\alpha'}(\mathbf{q}) &= \langle \hat{T} \delta \tilde{s}_\nu^\alpha(\mathbf{q}) \delta \tilde{s}_{\nu'}^{\alpha'}(\mathbf{q}) \rangle \\ &= \frac{1}{\beta} \sum_{\mathbf{R}} \int_0^\beta d\tau G_{\nu\nu'}^{\alpha\alpha'}(\mathbf{R}, \tau) e^{i\mathbf{k}\mathbf{R}+i\omega\tau}, \end{aligned} \quad (16)$$

where

$$\delta \tilde{s}^\alpha(\mathbf{q}) = \frac{1}{\beta\sqrt{N}} \sum_{\mathbf{j}} \int_0^\beta \delta \tilde{s}_{\mathbf{j}}^\alpha(\tau) e^{i\mathbf{k}\mathbf{j}+i\omega\tau} d\tau, \quad (17)$$

$$\delta \tilde{s}_{\mathbf{j}}^\alpha(\tau) = \frac{1}{\sqrt{N}} \sum_{\omega, \mathbf{k}} \delta \tilde{s}_{\mathbf{j}}^\alpha(\mathbf{k}, \omega) e^{-i\mathbf{k}\mathbf{j}-i\omega\tau} d\tau. \quad (18)$$

The unitary transformation (6) produces the connection between the Fourier images of the GF in the crystallographic and local XZ coordinates,

$$\begin{aligned} G_{\nu\nu}^{xx(zz)}(\mathbf{q}) &= \frac{1}{\gamma_\nu^2} \{ \Omega_\nu^2 \Gamma_{\nu\nu}^{XX}(\mathbf{q}) + h_\nu^2 \Gamma_{\nu\nu}^{ZZ}(\mathbf{q}) \\ &\pm h_\nu \Omega_\nu [\Gamma_{\nu\nu}^{ZX}(\mathbf{q}) + \Gamma_{\nu\nu}^{XZ}(\mathbf{q})] \}, \end{aligned} \quad (19)$$

$$\begin{aligned} G_{ab}^{xx(zz)}(\mathbf{q}) &= \frac{1}{\gamma_a \gamma_b} \{ \Omega_a \Omega_b \Gamma_{ab}^{XX}(\mathbf{q}) + h_a h_b \Gamma_{ab}^{ZZ}(\mathbf{q}) \\ &\pm [h_a \Omega_b \Gamma_{ab}^{ZX}(\mathbf{q}) + h_b \Omega_a \Gamma_{ab}^{XZ}(\mathbf{q})] \}, \end{aligned} \quad (20)$$

$$\begin{aligned} G_{ab}^{xz}(\mathbf{q}) &= \frac{1}{\gamma_a \gamma_b} \{ -h_a \Omega_b \Gamma_{ab}^{XX}(\mathbf{q}) + \Omega_a h_b \Gamma_{ab}^{ZZ}(\mathbf{q}) \\ &+ [h_a h_b \Gamma_{ab}^{XZ}(\mathbf{q}) - \Omega_a \Omega_b \Gamma_{ab}^{ZX}(\mathbf{q})] \}, \end{aligned} \quad (21)$$

$$\begin{aligned} G_{ab}^{zx}(\mathbf{q}) &= \frac{1}{\gamma_a \gamma_b} \{ -h_b \Omega_a \Gamma_{ab}^{XX}(\mathbf{q}) + \Omega_b h_a \Gamma_{ab}^{ZZ}(\mathbf{q}) \\ &+ [h_a h_b \Gamma_{ab}^{ZX}(\mathbf{q}) - \Omega_a \Omega_b \Gamma_{ab}^{XZ}(\mathbf{q})] \}. \end{aligned} \quad (22)$$

The Fourier transform of Green's function in the local XZ coordinate presented in Eqs. (19)-(22) are obtained analogously to Eqs. (15)-(16) using indexes λ, λ' ,

$$\Gamma^{\lambda\lambda'}(\mathbf{j} - \mathbf{j}', \tau - \tau') = \langle \hat{T} \delta \tilde{S}_{\mathbf{j}}^{\lambda}(\tau) \delta \tilde{S}_{\mathbf{j}'}^{\lambda'}(\tau') \rangle, \quad (23)$$

$$\begin{aligned} \Gamma^{\lambda\lambda'}(\mathbf{q}) &= \langle \hat{T} \delta \tilde{S}^{\lambda}(\mathbf{q}) \delta \tilde{S}^{\lambda'}(-\mathbf{q}) \rangle, \\ &= \frac{1}{\beta} \sum_{\mathbf{R}} \int_0^{\beta} d\tau \Gamma(\mathbf{R}, \tau) e^{i\mathbf{k}\mathbf{R} + i\omega\tau}. \end{aligned} \quad (24)$$

The GF in Eq. (24) is defined by

$$\Gamma^{\lambda\lambda'}(\mathbf{q}) = \frac{\langle \hat{T} \delta \tilde{S}^{\lambda}(\mathbf{q}) \delta \tilde{S}^{\lambda'}(-\mathbf{q}) \sigma(\beta) \rangle_0}{\langle \sigma(\beta) \rangle_0}, \quad (25)$$

where $\langle \dots \rangle_0 = \text{Tr}(e^{-\beta H_0} \dots) / \text{Tr}(e^{-\beta H_0})$ implies the thermodynamic average with the mean-field Hamiltonian in Eq. (7) and $\sigma(\beta) = \hat{T} \exp[-\int_0^{\beta} H_1(\tau) d\tau]$ is the scattering matrix. The Green's function matrix $\hat{\Gamma}(\mathbf{q})$ is presented by,

$$\begin{aligned} \hat{\Gamma}(\mathbf{q}) &= \begin{pmatrix} \hat{\Gamma}_{aa}(\mathbf{q}) & \hat{\Gamma}_{ab}(\mathbf{q}) \\ \hat{\Gamma}_{ba}(\mathbf{q}) & \hat{\Gamma}_{bb}(\mathbf{q}) \end{pmatrix} \\ &= \begin{pmatrix} \Gamma_{aa}^{XX}(\mathbf{q}) & \Gamma_{aa}^{XZ}(\mathbf{q}) & \Gamma_{ab}^{XX}(\mathbf{q}) & \Gamma_{ab}^{XZ}(\mathbf{q}) \\ \Gamma_{aa}^{ZX}(\mathbf{q}) & \Gamma_{aa}^{ZZ}(\mathbf{q}) & \Gamma_{ab}^{ZX}(\mathbf{q}) & \Gamma_{ab}^{ZZ}(\mathbf{q}) \\ \Gamma_{ba}^{XX}(\mathbf{q}) & \Gamma_{ba}^{XZ}(\mathbf{q}) & \Gamma_{bb}^{XX}(\mathbf{q}) & \Gamma_{bb}^{XZ}(\mathbf{q}) \\ \Gamma_{ba}^{ZX}(\mathbf{q}) & \Gamma_{ba}^{ZZ}(\mathbf{q}) & \Gamma_{bb}^{ZX}(\mathbf{q}) & \Gamma_{bb}^{ZZ}(\mathbf{q}) \end{pmatrix}. \end{aligned} \quad (26)$$

In Ref. [9], we developed a procedure to calculate $\hat{\Gamma}(\mathbf{q})$ in the Gaussian approximation using the functional integral representation for the scattering matrix, which is

$$\sigma(\beta) = \int D\psi \exp \left\{ -\frac{1}{2\beta} \sum_{\mathbf{q}\lambda\lambda'} I_{\lambda\lambda'}^{-1}(\mathbf{k}) \psi_{\lambda}(\mathbf{q}) \psi_{\lambda'}(-\mathbf{q}) \right\} \hat{T} \exp \left\{ \sum_{\lambda\mathbf{q}} \psi_{\lambda}(\mathbf{q}) \delta S^{\lambda}(\mathbf{q}) \right\}. \quad (27)$$

Here $I_{\lambda\lambda'}^{-1}(\mathbf{k})$ denotes the inverse matrix elements of $\hat{I}(\mathbf{k})$ indicated in Eq. (9). The functional integration over the complex field variable $\psi_\lambda(\mathbf{q}) = \psi_\lambda^c(\mathbf{q}) + i\psi_\lambda^s(\mathbf{q})$ takes the following form,

$$\begin{aligned} \int D\psi \dots &= \Pi_\lambda \int_{-\infty}^{\infty} \frac{d\psi_\lambda(0)}{\sqrt{2\pi \det[\beta \hat{I}(0)]}} \Pi_{\mathbf{q} \neq 0} \\ &\times \int_{-\infty}^{\infty} \frac{d\psi_\lambda^c(\mathbf{q})}{\sqrt{\pi \det[\beta \hat{I}(\mathbf{k})]}} \int_{-\infty}^{\infty} \frac{d\psi_\lambda^s(\mathbf{q})}{\sqrt{\pi \det[\beta \hat{I}(\mathbf{k})]}} \dots \end{aligned} \quad (28)$$

Here $\psi_\lambda^c(\mathbf{q})$ and $\psi_\lambda^s(\mathbf{q})$ are the real and imaginary parts of $\psi_\lambda(\mathbf{q})$, respectively and $\psi_\lambda^c(-\mathbf{q}) = \psi_\lambda^c(\mathbf{q})$, $\psi_\lambda^s(-\mathbf{q}) = -\psi_\lambda^s(\mathbf{q})$.

In the Gaussian approximation, Green's function $\hat{\Gamma}(\mathbf{q})$ satisfies the matrix equation:

$$\hat{\Gamma}(\mathbf{q}) = \hat{M}(\omega) [\hat{1} - \beta \hat{I}(\mathbf{k}) \hat{M}(\omega)]^{-1}, \quad (29)$$

where

$$\begin{aligned} \hat{M}(\omega) &= \begin{pmatrix} \hat{M}_a(\omega) & \hat{O} \\ \hat{O} & \hat{M}_b(\omega) \end{pmatrix}, \\ &= \begin{pmatrix} M_{aX}(\omega) & 0 & 0 & 0 \\ 0 & M_{aZ}(\omega) & 0 & 0 \\ 0 & 0 & M_{bX}(\omega) & 0 \\ 0 & 0 & 0 & M_{bZ}(\omega) \end{pmatrix}, \end{aligned} \quad (30)$$

and

$$M_{\nu X}(\omega) = \frac{b_s(y_\nu)}{y_\nu - i\omega\beta}, \quad (31)$$

$$M_{\nu Z}(\omega) = b'_s(y_\nu) \delta(\omega). \quad (32)$$

Here, the Brillouin function $b_s(y_\nu)$ and its derivative $b'_s(y_\nu)$ are given in Ref. [15].

Using Eqs.(9)-(12), (29)-(32), we evaluate the GFs $\Gamma^{\lambda\lambda'}(\mathbf{q})$ and insert them into Eqs. (19)-(22) to obtain the explicit expressions for the GFs in the original spin-lattice coordinate. Performing an analytic continuation, the transverse GF is written by

$$G_{aa}^{xx}(\mathbf{q}) = \frac{h_a^2 b_s(y_a)}{\gamma_a^2} \frac{(\gamma_b - J' \xi_{2\mathbf{k}} b_s(y_b) - \omega)}{(\omega - \epsilon_{\mathbf{k}}^+)(\omega - \epsilon_{\mathbf{k}}^-)}, \quad (33)$$

with the k-dependent poles $\epsilon_{\mathbf{k}}^\pm$ of the GF known as elementary excitation energies or magnons,

$$\begin{aligned} \epsilon_{\mathbf{k}}^\pm = & \frac{1}{2} \{ \gamma_a + \gamma_b - J' \xi_{2\mathbf{k}} [b_s(y_a) + b_s(y_b)] \} \\ & \pm \frac{1}{2} \sqrt{ \{ \gamma_a - \gamma_b - J' \xi_{2\mathbf{k}} [b_s(y_a) - b_s(y_b)] \}^2 + 4C^2 |\xi_{1\mathbf{k}}|^2 b_s(y_a) b_s(y_b) }. \end{aligned} \quad (34)$$

We note that the formula (34) better describes the temperature and field dependence of the magnon band structure compared with that obtained by Ref. [2]. To analyze the magnon spectrum in Eq. (34), we use the MFA result for magnetic moment per site derived from the unitary transformation in Eq. (6), which are

$$\begin{aligned} m_{\nu z} &= \frac{h_\nu b_s(y_\nu)}{\gamma_\nu}, m_{\nu x} = \frac{\Omega_\nu b_s(y_\nu)}{\gamma_\nu}, \\ m_\nu &= \sqrt{m_{\nu x}^2 + m_{\nu z}^2} = b_s(y_\nu), \\ m &= (m_a + m_b)/2, \\ y_\nu &= \beta \gamma_\nu. \end{aligned} \quad (35)$$

We can also obtain various elementary excitations (ferromagnetic, antiferromagnetic, ferromagnetic magnon) in the honeycomb spin-lattice using Eq. (34).

In the following parts, we concentrate only on ferromagnetic magnon which has been experimentally observed in the typical monolayer CrI₃ and the Van der Waals structures [5, 7].

3. Ferromagnetic magnon spectra in monolayer honeycomb spin-lattice

3.1. Ferromagnetic magnon in the application of transverse field at finite temperature

In this part, we examine the magnon spectra in the presence of the spin orientation (SR) effect by virtue of the TF. To emphasize the special role of the transverse field, the longitudinal field is supposedly turned off, $h_0 = 0$. The ferromagnetic (FM) magnon case corresponds to a homogeneous molecular field where $\gamma_a = \gamma_b \equiv \gamma$, $h = 3(J + 2J')m_z$, $\Omega = \Omega_0 + 3(L + 2J')m_x$ and $C = (J\Omega^2 + Lh^2)/\gamma^2$. Thus, the FM magnon spectrum is given by,

$$\epsilon_{\mathbf{k}}^{\pm} = \gamma - [J'\xi_{2\mathbf{k}} \mp C|\xi_{1\mathbf{k}}|]b_s(y). \quad (36)$$

Since $m = b_s(y)$, the positive spin-wave dispersion relation has two branches only when the net magnetic moment per site m is finite. At a given transverse field, the SR from the out-of-plane to an in-plane direction where $m_z = 0$, $m_x = m$ occurs at the SR temperature $\tau_R(\Omega_0)$ derived from the solution of the equation,

$$b_s\left(\frac{\Omega_0(J + 2J')}{\tau_R(J - L)}\right) = \frac{\Omega_0}{3(J - L)}, \quad (37)$$

with $\beta^{-1} = \tau$, $y = \gamma/\tau$. Similarly, the Curie temperature is extracted from Eq. (37) in the limit of zero TF,

$$\tau_c = \tau_R(\Omega_0 = 0) = s(s + 1)(J + 2J'). \quad (38)$$

In the presence of TF, the magnetic moment and the spin-wave energy follow different relations in certain temperature regions. Instead of Eq. (36), the energy spectrum of the FM magnon is explicitly expressed in different ranges of temperature which are

i/ Below the SR temperature ($0 < \tau < \tau_R(\Omega_0)$)

$$\begin{aligned} m_x &= \frac{\Omega_0}{3(J-L)}, m_z = \sqrt{b_s^2(y) - m_x^2}, \\ \gamma &= 3(J + 2J')b_s(y), y = \gamma/\tau. \end{aligned} \quad (39)$$

From that, the spin reorients from the out-of-plane to the in-plane direction at the SR field which is

$$\Omega_{0R}(\tau) = 3(J - L)b_s(y). \quad (40)$$

The magnon spectrum is then described by

$$\begin{aligned} \epsilon_{\mathbf{k}}^{\pm} &= b_s(y) \left\{ 3J + J'(6 - \xi_{2\mathbf{k}}) \right. \\ &\quad \left. \pm |\xi_{1\mathbf{k}}| \left[L + \frac{\Omega_0^2}{9(J-L)b_s^2(y)} \right] \right\}, \end{aligned} \quad (41)$$

where the zero-momentum magnon mode simplifies to,

$$\epsilon_0^{\pm} = 3b_s(y) \left\{ J \pm \left[L + \frac{\Omega_0^2}{9(J-L)b_s^2(y)} \right] \right\}. \quad (42)$$

At finite temperatures, the gap of the low-energy magnon branch at the center of the BZ closes, $\epsilon_0^- = 0$, when the transverse field reaches the SR field value in Eq. (40). In this case, the low-energy magnon branch is purely acoustic, which implies $\epsilon_{\mathbf{k}}^- \rightarrow 0$ when $\mathbf{k} \rightarrow 0$.

Near the Dirac point $\mathbf{K}'\left(\frac{2\pi}{3a_0}, -\frac{2\pi}{3\sqrt{3}a_0}\right)$, the magnon energy has a linear wave-vector dependence,

$$\epsilon^{\pm}(\mathbf{k}) \approx 3b_s(y)(J + 3J') \pm \hbar v_m |\mathbf{k} - \mathbf{K}'|. \quad (43)$$

The magnon speed v_m is a function of transverse field and temperature,

$$v_m = \frac{3b_s(y)a_0}{2\hbar} \left[L + \frac{\Omega_0^2}{9(J-L)b_s^2(y)} \right]. \quad (44)$$

ii/ Above the SR temperature ($\tau \geq \tau_R$),

The magnetization and the dispersion relation of magnon are correspondingly given by

$$\begin{aligned} m_z &= 0, \quad m_x = m = b_s(y'), \quad y' = \gamma'/\tau; \\ \gamma' &= \Omega_0 + 3(L + 2J')b_s(y'); \\ \epsilon_{\mathbf{k}}^{\pm} &= \Omega_0 + \left[3L + J'(6 - \xi_{2\mathbf{k}}) \pm J|\xi_{1\mathbf{k}}| \right] b_s(y'). \end{aligned}$$

Near the Dirac point K', $\epsilon_{\mathbf{k}}^{\pm} \approx \Omega_0 + (3L + 9J')b_s(y') \pm \hbar v'_m |\mathbf{k} - \mathbf{K}'|$ where the magnon speed is non-explicitly temperature and field dependent,

$$v'_m = \frac{3Ja_0b(y')}{2\hbar}. \quad (45)$$

iii/ At zero temperature

The spin reorientation is then interpreted as the quantum phase transition due to the TF. At zero temperature, the SR field equals the critical field $\Omega_{0R}(0) = \Omega_{0C}$. In this case, the Brillouin function reaches a saturated value, $b_s(y) = s$ with the spin moment per site s . Consequently, the critical transverse field causing QPT is (see Eq. (40))

$$\Omega_{0C} = \Omega_{0R}(0) = 3s(J - L). \quad (46)$$

The spin wave energy behaves differently depending on the transverse field, which is

a) $\Omega_0 \leq \Omega_{0C}$,

$$m_x = \frac{\Omega_0}{3(J-L)}, \quad m_z = s \sqrt{1 - \frac{\Omega_0^2}{\Omega_{0C}^2}}, \quad (47)$$

and the FM magnon follows a dispersion relation which is

$$\epsilon_{\mathbf{k}}^{\pm} = s \left\{ 3J + (6 - \xi_{2\mathbf{k}})J' \pm \left[L + \frac{\Omega_0^2}{9(J-L)s^2} \right] |\xi_{1\mathbf{k}}| \right\}, \quad (48)$$

where the zero-momentum magnon gaps at Brillouin zone center for two branches are

$$\epsilon_0^+ = 3s(J+L) + \frac{\Omega_0^2}{\Omega_{0C}}, \quad (49)$$

$$\epsilon_0^- = \Omega_{0C} \left(1 - \frac{\Omega_0^2}{\Omega_{0C}^2} \right). \quad (50)$$

It is obviously seen from Eq. (50) that the low-energy branch magnon gap closes at the critical field Ω_{0C} .

b) $\Omega_0 \geq \Omega_{0C}$

The magnetization is simplified to $m_z = 0$, $m_x = s$ and the magnon spectrum linearly varies on the TF, which is

$$\epsilon_{\mathbf{k}}^{\pm} = \Omega_0 + s[3L + J'(6 - \xi_{2\mathbf{k}}) \pm J|\xi_{1\mathbf{k}}|]. \quad (51)$$

3.2. Numerical results

For numerical calculations, energy-dependent quantities such as FM-magnon energy $\epsilon^{\pm}(\mathbf{k})$, temperature τ ; parameters L, J' ; field strength γ, h, Ω are measured in terms of NN exchange J and lengths are expressed in terms of a_0 .

Fig. 2(a) illustrates the MF thermomagnetic behaviors by using Eqs. (37)-(39), when $\Omega_0=0$ and 0.8, $L = 0.4$, $J' = 0.1$, $s = 3/2$. The reduction of the spin reorientation temperature τ_R with increasing transverse field is exhibited in Fig. 2(b). The Curie temperature $\tau_C = 4.5$ is obtained as the spin reorientation temperature when $\Omega_0 = 0$ according to Eq. (38). At the critical value $\Omega_{0C} = 2.7$, the SR temperature becomes zero.

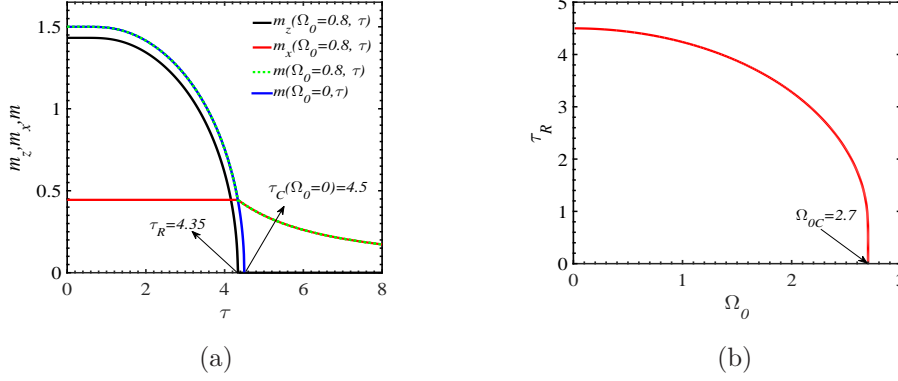


Figure 2: Temperature dependence of the magnetic moment per site m and its component m_x, m_z of the FM monolayer honeycomb spin-lattice in the transverse field $\Omega_0 = 0$ and 0.8 (a), and change of spin reorientation temperature with increasing transverse field (b). Here $s=3/2$, $L=0.4$, $J'=0.1$.

Two magnon branches $\epsilon^\pm(\mathbf{k})$ are displayed in Fig. 3(a)-(c) at temperature $\tau = 1.2$ (lower than the SR temperature) over the Brillouin zone while the cross-section along the $\Gamma\text{K}\text{M}\Gamma$ line are presented in Fig. 3(d)-(f), respectively. The magnon energy at the Dirac K point increases strongly when increasing the NNN interaction J' from 0.1 to 0.5. The magnon spectra shown in Fig. 3(e), (f) are quite similar to the DFT calculation result for the adiabatic magnon energy of CrI_3 (see Fig. 8(a) in Ref. [16]).

The difference between the magnon branches along the $\Gamma\text{M}\text{K}\Gamma$ line outside the Dirac K-point increases when the transverse field Ω_0 increases with $J' = 0.1$ and 0.5 in the temperature region below τ_R (see Fig. 4). Meanwhile, the upper FM–magnon band curvature near the M point changes from upward to downward with increasing Ω_0 . This implies that the sign of the effective mass of the upper FM–magnon branch is adjustable by the transverse field.

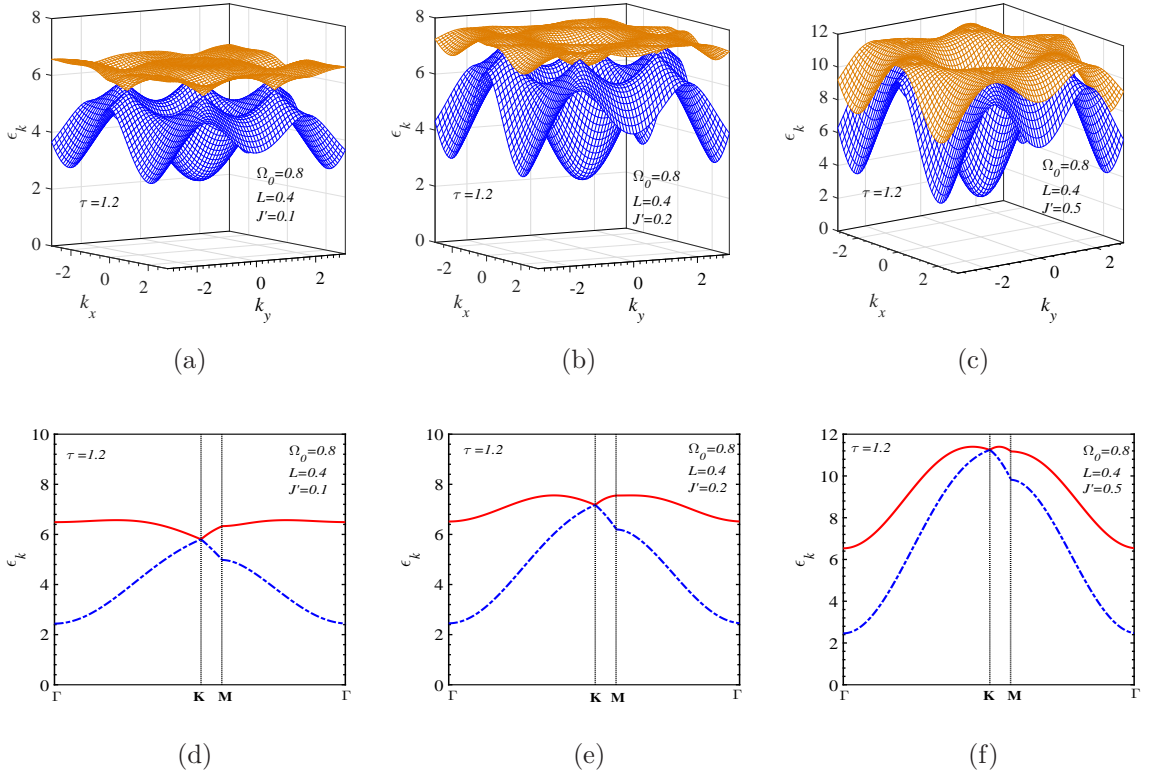


Figure 3: FM magnon spectral branches over the whole Brillouin zone with different NNN interaction $J'=0.1$ (a), 0.2 (b), 0.5 (c). Here transverse field $\Omega_0 = 0.8$, $s = 3/2$, $L = 0.4$, $\tau = 1.2$. The magnon energy spectrum along the Γ MK Γ line with the same parameters in the (a)-(c) cases are illustrated in (d)-(f) cases, correspondingly.

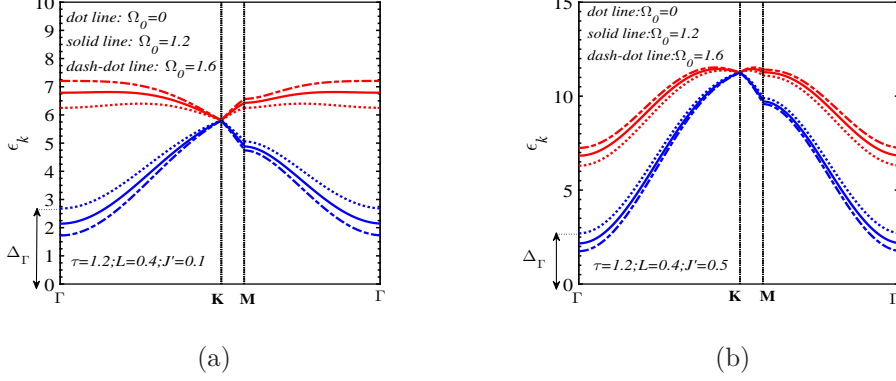


Figure 4: Wave-vector dependence of the magnon branches along the $\Gamma\text{MK}\Gamma$ line with increasing transverse field $\Omega_0 = 0, 1.2, 1.6$. Parameters are chosen as $s = 3/2$, $\tau = 1.2$, $L = 0.4$, and $J' = 0.1$ (a), 0.5 (b).

As also mentioned in Ref. [17], the energy gap of the low-energy magnon branch at the Γ point (Δ_Γ or ϵ_0^-) has an anisotropy origin and does not depend on J' (see Eq. (41)). This gap is proportional to the TR field as a function of Ω_0^2 and reduces with increasing TR from 0 to 1.6.

Fig. 5 exhibits the magnon branches along the $\Gamma\text{KMF}\Gamma$ line at very low temperature $\tau = 0.001$. At the center of the Brillouin zone, or the Γ point, the upper FM–magnon branch bottom shifts to the higher value with increasing the transverse field, and the gap of the low-energy FM–magnon branch closes when the transverse field approaches the spin reorientation field $\Omega_{0R} = 2.7$. The temperature dependence of the zero-momentum FM–magnon spectra $\epsilon_{\mathbf{k}}(\mathbf{k} = \mathbf{0})$ in Fig. 6(a), (c) indicates that two branches of these spectra change discontinuously at the SR temperature corresponding to the step-change of the incline angle of the spin direction above the single-layer spin plane as seen in Fig. 6(b), (d). For the case of Fig. 6(a) ($L = 0.05$, $J' = 0.1$), our model

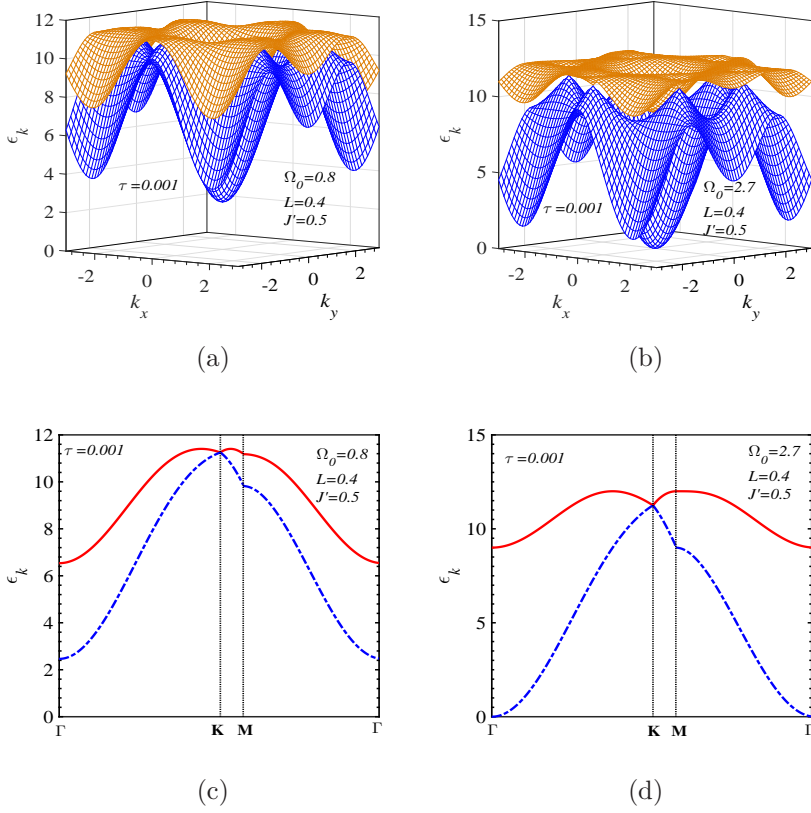


Figure 5: FM–magnon branches over the whole Brillouin zone with increasing transverse field $\Omega_0 = 0.8$ (a) and 2.7 (b). Here $s = 3/2$, $L = 0.4$, $\tau = 0.001$, $J' = 0.5$. The magnon energy spectrum along the Γ MKT line with the same parameters in the (a) and (b) cases are illustrated in (c) and (d), respectively.

is analogous to the Ising model where the zero-momentum magnon energies of two branches are weak temperature-dependent in the temperature region above τ_R . This realization was also experimentally observed in Ref. [8].

The influence of temperature on the behavior of the magnon energy is unveiled in Fig. 7 where a disrupt change of $\epsilon_{\mathbf{k}}$ occurs at the SR temperature. At a certain transverse field, the difference between the two magnon branches depends on the intrinsic parameters L , J' , s , and the wave vector. For the same set of parameters, $\Omega_0 = 0.8$, $L = 0.4$, $J' = 0.1$, $s = 3/2$, this difference is more pronounced for the wave vector at or near the center of the Brillouin zone ($k_x = k_y = 0.5$ in Fig. 7(b)) than for the \mathbf{k} value near the Dirac points ($k_x = 1.89$; $k_y = 1.01$ in Fig. 7(c)). Moreover, it is also indicated that a possible temperature gap opens for the non-zero-momentum low-energy magnon branch. In other words, this branch can not vanish in a wide range of temperatures.

At zero temperature $\tau = 0$ where the SR transition is considered as the QPT with the tuning parameter Ω_0 , we are interested in the energy variation of several magnon modes with various transverse field Ω_0 . The gap between two branches of the zero-momentum FM–magnon energy shown in Fig. 8(a) increases proportionally to Ω_0^2 when $\Omega_0 \leq \Omega_{0C}$ and reaches the maximum value of $6s$ for $\Omega_0 \geq \Omega_{0C}$. It is emphasized that the zero-momentum magnon branch cuts the horizontal axis in Fig. 8(a) at the critical transverse field Ω_{0C} . The low-energy magnon branch mode at other points of Brillouin zone ($\mathbf{k} \neq \mathbf{0}$) including points near the Dirac one ($k_x = 1.89$; $k_y = 1.01$ in Fig. 8(b)) is always finite for any TF value. The gap between two magnon branches remains constant when the TF intensity is larger than the critical

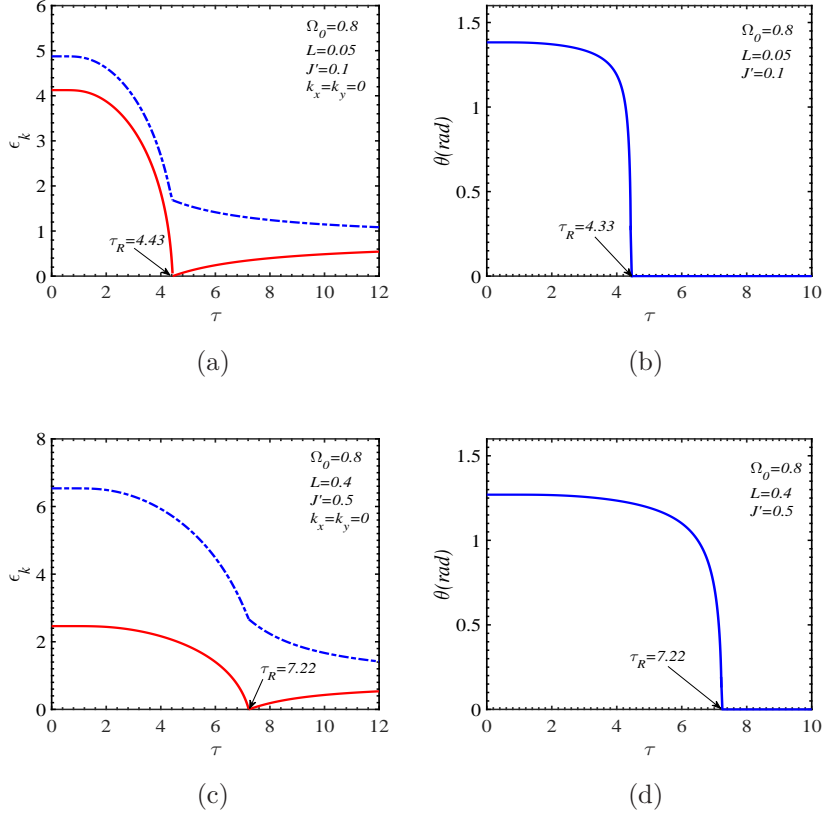


Figure 6: The zero-momentum ($\mathbf{k} = 0$) spin-wave energy and the decline angle θ of magnetic-moment vector versus temperature in the transverse field $\Omega_0 = 0.8$. Other parameters are chosen as $L = 0.05$, $J' = 0.1$ for (a) and (c); $L = 0.4$, $J' = 0.5$ for (b) and (d). Arrows indicate the SR temperatures. Here the spin value is taken $s = 3/2$.

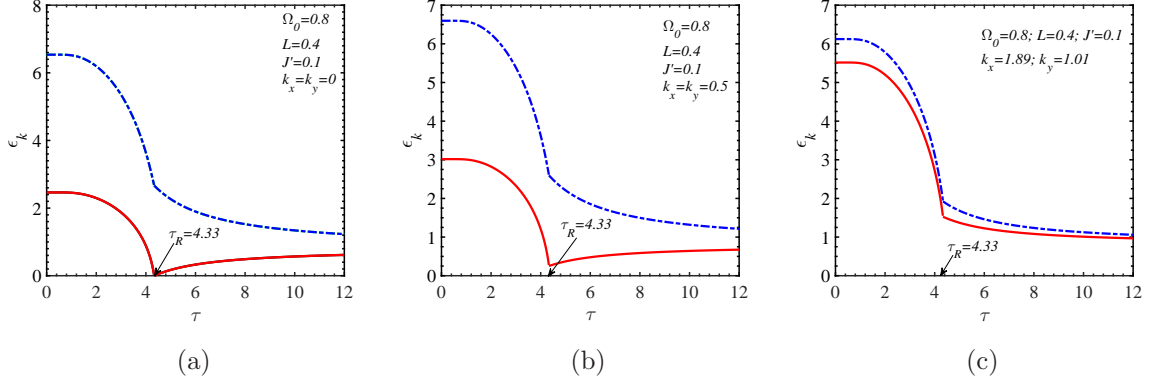


Figure 7: The discontinuous change of the FM magnon spectrum at the SR temperature when $k_x = k_y = 0$ (a); $k_x = k_y = 0.5$ (b); $k_x = 1.89, k_y = 1.01$ (c). Here we choose $\Omega_0 = 0.8, L = 0.4, J' = 0.1, s = 3/2$.

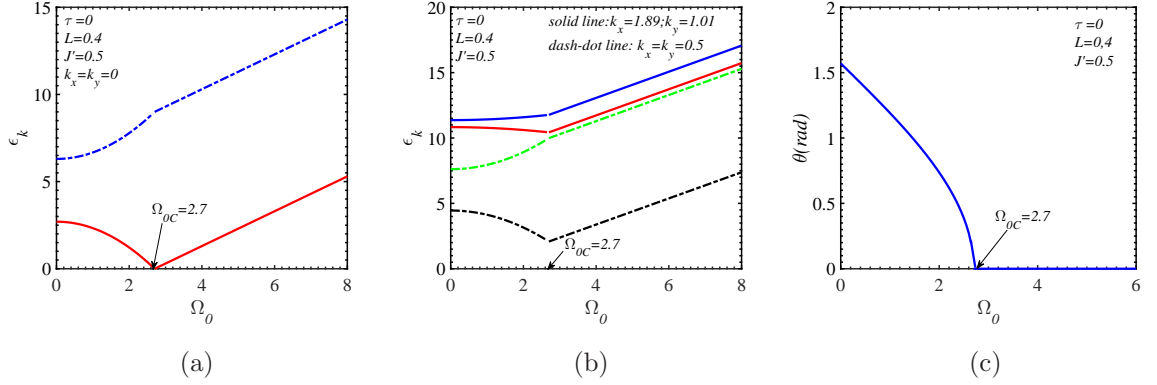


Figure 8: The magnon energy modes at different points of the Brillouin zone where $k_x = k_y = 0$ (a); $k_x = k_y = 0.5$ and $k_x = 1.89, k_y = 1.01$ (b), and the inclined angle of the magnetic moment versus the transverse field (c). Here we choose $L = 0.4, J' = 0.5, s = 3/2$.

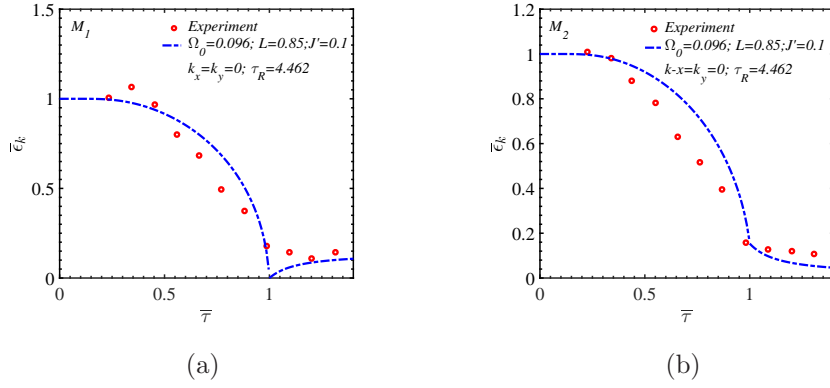


Figure 9: The comparison between theory and experiment [8] for the temperature dependence of the zero-momentum magnon mode M_1 (a) and M_2 (b). The quantities $\bar{\epsilon}_k$, $\bar{\tau}$ are relative magnon energy and relative temperature (see the text). Fitted parameters and the SR temperature τ_R are given in terms of J .

tuning parameter Ω_{0C} due to the linear dependence on the TF displayed in Eq. (51). We also present in Fig. 8(c) the change of the inclined angle of the spin direction θ with different TF Ω_0 . Both the inclined angle and the SR temperature disappear at the critical field $\Omega_{0C} = 2.7$ (see also Fig. 2(b)).

3.3. Estimation for CrI_3 monolayer

A ferromagnetic order with an out-of-plane spin orientation was experimentally observed in the CrI_3 monolayer. The temperature dependence of the integrated intensity of the M_1 and M_2 magnon modes performed in Ref. [8] was carried out on 13-layer films. To apply the single layer model for this CrI_3 thin film, we propose an out-of-plane magnetic moment with an initial incline angle of the film plane caused by the competition between anisotropic exchanges and TF fields. The effective anisotropy originated from the transverse strain in 2D materials plays the role of the transverse field in the model.

The presence of the magnon mode intensity above SR temperature is an evidence of the transverse field.

Fig. 9 shows the theoretical fit with the experimental data for the temperature dependence of the zero-momentum M_1 and M_2 magnon modes in CrI_3 [8]. Here, the ratio of zero-momentum magnon energy at finite temperatures to this at zero temperature and relative temperature are denoted as $\bar{\epsilon}_{\mathbf{k}} = \epsilon_{\mathbf{k}}(T)/\epsilon_{\mathbf{k}}(0)$ and $\bar{\tau} = T/T_R$, respectively. The fitted theoretical parameters presented in terms of the out-of-plane exchange constant J are $J' = 0.1$; $L = 0.85$; $\Omega_0 = 0.096$; $\tau_R = 4.462$ where the SR temperature τ_R approximates to the Curie temperature $\tau_C = 4.5$ estimated by Eq. 38. Using the experimental value of the SR temperature of CrI_3 monolayer in Ref. [8], $\tau_R = 45$ K, we obtain $J = 0.869$ meV, the in-plane NN exchange constant $L = 0.739$ meV, the isotropic NNN exchange constant $J' = 0.087$ meV and the transverse field $\Omega_0 = 0.083$ meV. We also make a comparison of these exchange parameters obtained from the DFT calculations for the CrI_3 monolayer [13, 18, 16] with our present work and with the 13-layer film data using NN anisotropic Heisenberg model [8]. The data of different works are listed in Table 1.

We can see that the NN exchange parameter J of our work is in good agreement with the DFT derivations in Ref. [18, 16] and the evaluation of the Ref. [8] is too high. Taking $\Omega_0 = g\mu_B B_{0x}$ where the Bohr magneton $\mu_B = 5.788 \times 10^{-5}$ eV/T and the g-factor of the ion Cr^{3+} is 1.98 [19], we estimate the transverse field for the 13-layer CrI_3 film, $B_{0x} = 0.73$ T. This value is in the interval of the in-plane saturated field for the CrI_3 monolayer (~ 0.17 T) and for the bulk (~ 2 T) [8]. Using the lattice constant $a_0 = 6.867 \times 10^{-10}$

Table 1: The magnitude of the out-of-plane NN, in-plane NN, NNN exchanges J, L, J' exchange parameters obtained by different works, respectively.

Parameter (meV)	Present work	Ref. [16]	Ref. [13]	Ref. [18]	Ref. [8]
J	0.869	1.025	1.53	0.72	5.46
L	0.739	-	-	-	1.36
J'	0.087	0.549	0.38	-	-

m extracted in Ref. [20] and the formula (44), we readily obtain the magnon velocity in the 2D CrI₃ near Dirac point and at zero temperature $v_m = 1.74$ km/s. We are looking forward to experimental data to compare with this value.

4. Conclusion

The temperature and the field dependence of the ferromagnetic magnon spectra in the honeycomb single-layer spin film are calculated using the anisotropic exchange XZ-Heisenberg model with the transverse field. The field and temperature dependence of the magnetization are examined within the mean-field approximation while the magnon energy is calculated by using the Gaussian approximation. The finite-temperature phase transition due to the TF is the spin reorientation transition in the monolayer honeycomb spin-lattice with the initial out-of-plane magnetization. The collective excitation follows the different dispersion relations below or above the SR temperature. The transverse-field dependence of the magnon spectrum at zero temperature corresponding to QPT is also illustrated and the gap of the zero-momentum

low-energy magnon branch disappears at the critical QPT field. The model application for the magnon modes in the 2D-CrI₃ ferromagnet reveals a suitable agreement.

Acknowledgment

We would like to thank the grant Nafosted 103.01-2019.324 for support.

References

- [1] T. O. Wehling, A. M. Black-Schaffer and A. V. Balatsky, *Adv. Phys.* **63**, 1 (2014).
- [2] J. Fransson, A. M. Black-Schaffer, and A. V. Balatsky, *Phys. Rev. B* **94**, 075401 (2016).
- [3] S. Peshoguba, S. Banerjee, J. C. Lashley, J. Park, H. Agren, G. Aepli, and A.V. Balatsky, *Phys. Rev. X* **8**, 011010 (2018).
- [4] D. Boyko, A. V. Balatsky, J. T. Haraldsen, *Phys. Rev. B* **97**, 014433 (2018).
- [5] B. Huang, G. Clark, E. Navarro-Moratalla et al, *Nature* **546**, 270 (2017).
- [6] M. Gilbertini, M. Koperski, A. F. Morpurgo and K. S. Novoselov, *Nat. Nanotechnol.* **14**, 408 (2019).
- [7] J. Cenker, B. Huang, N. Suri et al, *Nat. Phys.* **17**, 20 (2021).
- [8] W. Jin, H. H. Kim, Z. Ye, S. Li, P. Rezaie, F. Diaz, S. Siddiq, E. Wauer, B. Yang, C. Li, S. Tian, K. Sun, H. Lei, A. W. Tsen, L. Zhao, R. He, *Nat. Commun.* **9**, 5122 (2018).

- [9] Niem T. Nguyen, Thao H. Pham, Giang H. Bach, and Cong T. Bach, Mater. Trans. **59**, 1075 (2018).
- [10] S. Schwieger, J. Kienert, and W. Nolting, Phys. Rev. B **71**, 024428 (2005).
- [11] J. F. Scott, A. Schilling, S. E. Rowley, and J. M. Gregg, Sci. Technol. Adv. Mater. **16**, 036001 (2015).
- [12] S. Li, Z. Ye, X. Luo, G. Ye, H. H. Kim, B. Yang, S. Tian, C. Li, H. Lei, A. W. Tsen, K. Sun, R. He, and L. Zhao, Phys. Rev. X **10**, 011075 (2020).
- [13] M. Pizzochero, O. V. Yazyev, J. Phys. Chem. C **124**, 7585 (2020).
- [14] N. D. Mermin, H. Wagner, Phys. Rev. Lett. **17**, 1133 (1966).
- [15] Cong T. Bach, Niem T. Nguyen, Giang H. Bach, Jour. Magn. Magn. Mater. **483**, 136 (2019).
- [16] D. Wang and B. Sanyal, J. Phys. Chem. C **125**, 18467 (2021).
- [17] A. T. Costa, D. L. R. Santos, N. M. R. Peres and J. Fernandez-Rossier, 2D Mater. **7**, 045031 (2020).
- [18] M. Pizzochero, R. Yadav, and O.V. Yazyev, 2D Mater. **7**, 035055 (2020).
- [19] C.L. Saiz, M. A. McGuire, S.R.J. Hennadige et. al., MRS Advances **4**, 2169 (2019).
- [20] M. A. McGuire, H. Dixit, V. R. Cooper, and B. C. Sales, Chem. Mater. **27**, 612 (2015).